Simulation of nanoparticle coagulation in radio-frequency capacitively coupled C_2H_2 discharges*

Liu Xiang-Mei(刘相梅)[a)†], Li Qi-Nan(李奇楠)[a)], and Xu Xiang(徐 翔)[b)]

[a)] *School of Science, Qiqihar University, Qiqihar* 161006, *China*

[b)] *School of Physics and Optoelectronic Technology, Dalian University of Technology, Dalian* 116024, *China*

(Received 27 November 2013; revised manuscript received 28 January 2014; published online 20 June 2014)

A self-consistent fluid model is employed to investigate the coagulation stage of nanoparticle formation, growth, charging, and transport in a radio-frequency capacitively coupled parallel-plate acetylene (C_2H_2) discharge. In our simulation, the distribution of neutral species across the electrode gap is determined by mass continuity, momentum balance, and energy balance equations. Since a thermal gradient in the gas temperature induced by the flow of the neutral gas, a careful study of the thermophoretic force on the spatial distribution of the nanoparticle density profiles is indispensable. In the present paper, we mainly focus on the influences of the gas flow rate, voltage, and gas pressure on the spatial distribution of the nanoparticle density. It appears that the resulting density profile of the 10-nm particles experiences a significant shift towards the upper showerhead electrode once the neutral equations are applied, and a serious shift is observed when increasing the gas flow rate. Thus, the flow of neutral gas can strongly influence the spatial distribution of the particles in the plasma.

Keywords: nanoparticle dynamics, acetylene discharges, numerical simulation

PACS: 52.27.Lw, 52.65.–y, 52.80.pi **DOI:** 10.1088/1674-1056/23/8/085202

1. Introduction

Radio-frequency (RF) powered plasma-enhanced chemical vapor deposition (PECVD) is often used to deposit hydrogenated amorphous carbon a-C:H thin films, which are applied in tribological materials,[1,2] passivation layers,[3] and field emission cold cathodes for future flat-screen displays.[4–6] Among these applications, the formation and growth of nanosize particles are critical issues. It was found that the presence of nanoparticles in amorphous carbon thin films can effectively enhance electron emission,[1,2] making them a promising material for the fabrication of field electron emitters. Therefore, it is essential to understand the formation, growth, charging, and transport of nanoparticles in acetylene plasma discharges. Recently, different models have been used to study the formation of nanoparticles. Doyle and Herrebout *et al.*[7,8] analyzed the basic reaction mechanisms of small species in a typical RF acetylene plasma; however, some ion–neutral reactions have not been taken into account and many assumptions are made in their model. Stoykov *et al.*[9] did consider the growth of linear chain and cyclic hydrocarbon molecules containing up to ten carbon atoms, but assumed a constant positive ion concentration and the role of positively charged hydrocarbon clusters was not investigated. To reveal the underlying dust formation mechanisms and the most important precursors of the dust formation in RF acetylene plasma, De Bleecker *et al.*[10] developed a detailed model for describing the chemical kinetic scheme, involving electron impact, neutral–neutral, and ion–neutral reactions. Noted that when comparing these results with experimental measurement by Deschenaux *et al.*[11] and Benedikt *et al.*,[8] there was not yet a satisfying agreement for negative ions. Recently, to obtain a more realistic picture of the important pathways for nanoparticle formation in acetylene plasmas, Mao *et al.*[12] proposed some new mechanisms for negative ion formation and growth, and a reasonable agreement is achieved between the calculated results and experimental measurement. From their results, we can obtain a comprehensive understanding of the initial mechanisms of nanoparticle formation.

Till now, few works have been focused on the coagulation phase with a sectional model in acetylene discharge. However, coagulation in nanodusty plasmas plays an important role in the nanoparticle growth process and has been paid much attention.[13,14] This is because coagulation can strongly affect the particle morphology, and which has implications for the deliberate synthesis of nanocrystals for various applications. Moreover, by coagulation, particles can grow to several tens of nanometers in diameter following their initial formation via gas-phase nucleation and even acquire a charge, which depends on the particle size. Therefore, investigations of nanoparticle growth mechanisms in the coagulation phase are very necessary in acetylene plasma discharges.

In this work, we extend our previously developed one-dimensional (1D) fluid model[15] by adding the neutral equa-

*Project supported by the China Postdoctoral Science Foundation (Grant No. 2012M511603), the National Natural Science Foundation of China (Grant Nos. 11105057 and 10775025), and the Fundamental Research Funds for the Central Universities of China (Grant No. DUT12LK39).

†Corresponding author. E-mail: lxmjsc98@163.com

© 2014 Chinese Physical Society and IOP Publishing Ltd

tions including mass continuity, momentum balance, and energy balance, especially the neutral gas energy balance equation, since thermophoresis can be a very dominant force that can strongly influence the spatial distribution of the particles in the nanometer area.[16] This paper is organized as follows: in Section 2, an overview of the model is given, including a detailed model description of neutral gas and dust particles. The numerical results are discussed and analyzed in Section 3. Finally, the conclusion is given in Section 4.

2. Theoretical model

In this way, we used a sectional model to simulate the growth of nanoparticles in a RF acetylene discharge, which self-consistently coupled to a plasma fluid model, including a solution of Poisson's equation for the electric field. In recent years, the quantum hydrodynamics model has received wide attention for the important applications in laser-plasmas,[17] thin metal films,[18] and electrons in metals.[19] However, compared to the quantum hydrodynamics model, the fluid model has the advantages of short time consumption and high precision, which is of important for nanoparticle formation. The following are the main aspects of the fluid model. For every species j (electrons, ions), a density balance equation is taken into account. The electron momentum equation is estimated by drift-diffusion approximation, as the characteristic length for the discharge chamber is much longer than the mean free-path of electron–neutral collisions. Furthermore, an energy balance equation for electrons is incorporated, which includes the Ohmic heating and the loss of energy due to electron impact collisions. For ions, the momentum equation is applied to study the ion velocity. It is worth mentioning that the ion pressure plays only a minor role in the momentum equation, then we assume that the pressure force for ions can be characterized by a scalar temperature $T_{\rm i}$. Thus, the ion temperature $T_{\rm i}$, which is assumed to be a constant and of the order of the temperature of the parent neutral species, can hardly affect the results in any case.[20] Moreover, since the ion temperature is much smaller than the electron temperature, the ion movement can be described by the "cold fluid" model. In this case, the momentum balance equation is replaced by the drift-diffusion approximation. An effective electric field is used to follow the instantaneous electric field. By adopting this effective electric field, the inertia effects of the ions are taken into account.

For neutrals species, a neutral reacting flow is investigated by the mass continuity equation, which solves the interchangeable mass density $n_{\rm n}$ and the momentum balance equation that solves the axial mass-averaged velocity $\boldsymbol{u}_{\rm n}$,

$$\frac{\partial n_{\rm n}}{\partial t}+\nabla\cdot n_{\rm n}\boldsymbol{u}_{\rm n}=R_{\rm n}, \tag{1}$$

$$\frac{\partial n_{\rm n}m_{\rm n}\boldsymbol{u}_{\rm n}}{\partial t}+\nabla\cdot(n_{\rm n}m_{\rm n}\boldsymbol{u}_{\rm n}\boldsymbol{u}_{\rm n})=-\nabla p_{\rm n}-\nabla\cdot\boldsymbol{\Pi}_{\rm n}+\boldsymbol{M}_{\rm n}, \tag{2}$$

where $R_{\rm n}$ describes all the different production and loss terms of the neutral gas, $\boldsymbol{M}_{\rm n}$ are the transfer of mass to the neutral gas fluid by collisions with other species, and $m_{\rm n}$, $p_{\rm n}$ are the mass and pressure of the neutral gas. A Newtonian form is assumed for the neutral viscous stress tensor $\boldsymbol{\Pi}_{\rm n}$,[21] which can be written as

$$\nabla\cdot\boldsymbol{\Pi}_{\rm n}=\eta_{\rm n}\left[\nabla^2\boldsymbol{u}_{\rm n}+\frac{1}{3}\nabla(\nabla\cdot\boldsymbol{u}_{\rm n})\right], \tag{3}$$

where $\eta_{\rm n}$ is the viscosity coefficient. Since thermal particle motion is taken into account in the present model, the viscosity term, which arises from the non-diagonal components of the pressure tensor, can be considered as momentum diffusion, with $\eta_{\rm n}$ playing the role of a diffusion coefficient.

The neutral gas energy balance, that solves the neutral temperature $T_{\rm n}$ is given by

$$\frac{\partial}{\partial t}(n_{\rm n}C_{\rm v}T_{\rm n})+\nabla\cdot(n_{\rm n}C_{\rm v}T_{\rm n}\boldsymbol{u}_{\rm n})=-\nabla\cdot\boldsymbol{q}_{\rm n}-p_{\rm n}\nabla\cdot\boldsymbol{u}_{\rm n}+E_{\rm n}, \tag{4}$$

$C_{\rm v}$ represents the heat capacity at constant volume, $\boldsymbol{q}_{\rm n}$ is the neutral heat flux vector, and $E_{\rm n}$ represents the energy transfer to the neutral species by collisions with other species.

In this paper, a total of 57 different species j (electrons, ions, neutrals, and radicals) is taken into account which are: C_2H_2, C_4H_2, C_6H_2, C_8H_2, $C_{10}H_2$, $C_{12}H_2$, H_2, $C_6H_2^*$, $C_8H_2^*$, $C_{10}H_2^*$, CH, CH_2, H, C_2H, C_4H, CH_2, C_6H, C_8H, $C_{10}H$, $C_{12}H$, C_8H_6, $C_{10}H_6$, $C_{12}H_6$, $C_2H_2^+$, C_2H^+, CH^+, C_2^+, C^+, C_4H^+, C_6H^+, C_8H^+, $C_4H_2^+$, $C_6H_2^+$, $C_8H_2^+$, $C_4H_2^+$, $C_6H_2^+$, $C_8H_2^+$, $C_6H_4^+$, $C_8H_4^+$, $C_8H_6^+$, $C_{10}H_6^+$, $C_{12}H_6^+$, H_2^+, H^+, C_2H^-, C_4H^-, C_6H^-, C_8H^-, $C_{10}H^-$, $C_{12}H^-$, H_2CC^-, $C_4H_2^-$, $C_6H_2^-$, $C_8H_2^-$, $C_8H_4^-$, $C_{10}H_4^-$, e. The electron impact collisions reactions, which represent the earliest stages of particle formation, are given in Table 1.

Different from charged particles, the nanoparticles are also affected by other forces, including neutral drag, ion drag, gravity, and thermophoresis, which can strongly affect the nanoparticles transport besides the electrostatic force. Once we assume that the damping neutral drag balances the sum of all other forces, the nanoparticles flux term $\Gamma_{\rm d}$ can also be described as a kind of drift-diffusion expression[10]

$$\begin{aligned}\Gamma_{\rm d} =& -\mu_{\rm d}n_{\rm d}E_{\rm eff}-D_{\rm d}\frac{{\rm d}n_{\rm d}}{{\rm d}x}-\frac{n_{\rm d}}{v_{\rm md}}g\\&+\sum\frac{n_{\rm d}m_{\rm i}\upsilon_{\rm s}}{m_{\rm d}v_{\rm md}}\left(4\pi b_{\pi/2}^2\Gamma+\pi b_{\rm c}^2\right)\Gamma_{\rm i}\\&-\frac{32}{15}\frac{n_{\rm d}r_{\rm d}^2}{m_{\rm d}v_{\rm md}\upsilon_{\rm th}}k_{\rm T}\frac{{\rm d}T_{\rm gas}}{{\rm d}x},\end{aligned} \tag{5}$$

where $n_{\rm d}$, $r_{\rm d}$, $Q_{\rm d}$ are the nanoparticle's density, radius, and charge, g is the gravitational acceleration, $k_{\rm T}$ represents the translation part of the thermal conductivity, and $\upsilon_{\rm s}$, $\upsilon_{\rm th}$ are the mean speed and the average thermal velocity of

Table 1. Electron impact collisions included in the model and their corresponding threshold energies.

Reaction	Threshold energy/eV	Reaction type	Reference
$e + C_2H_2 \rightarrow C_2H_2^+ + 2e$	11.4	ionization	[12]
$e + C_2H_2 \rightarrow C_2H^+ + H + 2e$	16.5	dissociative ionization	[12]
$e + C_2H_2 \rightarrow C_2^+ + H_2 + 2e$	17.5	dissociative ionization	[12]
$e + C_2H_2 \rightarrow CH^+ + CH + 2e$	20.6	dissociative ionization	[12]
$e + C_2H_2 \rightarrow C^+ + CH_2 + 2e$	20.3	dissociative ionization	[12]
$e + C_2H_2 \rightarrow H^+ + C_2H + 2e$	18.4	dissociative ionization	[12]
$e + C_2H_2 \rightarrow C_2H + H + e$	7.5	dissociative	[12]
$e + C_2H_2 \rightarrow C_2H^- + H$	2.74	dissociative	[12]
$e + H_2 \rightarrow H_2^+ + 2e$	15.4	ionization	[12]
$e + H_2 \rightarrow H + H + e$	8.9	dissociative	[12]
$e + C_4H_2 \rightarrow C_4H + H + e$	7.5	dissociative	[12]
$e + C_6H_2 \rightarrow C_6H + H + e$	7.5	dissociative	[12]
$e + C_8H_2 \rightarrow C_8H + H + e$	7.5	dissociative	[12]
$e + C_{10}H_2 \rightarrow C_{10}H + H + e$	7.5	dissociative	[12]
$e + C_{12}H_2 \rightarrow C_{12}H + H + e$	7.5	dissociative	[12]
$e + C_4H_2 \rightarrow C_4H_2^+ + 2e$	10.19	ionization	[12]
$e + C_6H_2 \rightarrow C_6H_2^+ + 2e$	9.55	ionization	[12]
$e + C_2H_2 \rightarrow H_2CC^-$	2.74	attachment	[12]
$e + C_4H_2 \rightarrow C_4H^- + H$	1.94	dissociative attachment	[12]
$e + C_6H_2 \rightarrow C_6H^- + H$	2.74	dissociative attachment	[12]
$e + C_8H_2 \rightarrow C_8H^- + H$	2.74	dissociative attachment	[12]
$e + C_{10}H_2 \rightarrow C_{10}H^- + H$	2.74	dissociative attachment	[12]
$e + C_6H_2^* \rightarrow C_6H^- + H$	2.74	dissociative attachment	[12]
$e + C_8H_2^* \rightarrow C_8H^- + H$	2.74	dissociative attachment	[12]
$e + C_{10}H_2^* \rightarrow C_{10}H^- + H$	2.74	dissociative attachment	[12]

the background gas, respectively. The nanoparticles mobility $\mu_d = Q_d/m_d\nu_{md}$, the nanoparticles diffusion coefficient $D_d = \mu_d k_B T_n/Q_d$, and the momentum loss frequency $\nu_{md} = \sqrt{2}(P_{tot}/K_B T_n)\pi r_d^2\sqrt{8k_B T_n/\pi m_d}$. The Coulomb logarithm

$$\Gamma = \frac{1}{2}\ln\left(\frac{\lambda_L^2 + b_{\pi/2}^2}{b_c^2 + b_{\pi/2}^2}\right), \tag{6}$$

where b_c represents the collection parameter, $b_{\pi/2}$ is the impact parameter corresponding to the deflection angle $\pi/2$. A continuum equation based on Ref. [13] describing the spatial and temporal variation of nanoparticle concentration n_d for nanoparticles is shown in Eq. (7),

$$\frac{dn_d}{dt} + \frac{d\Gamma_d}{dx} = J_{nuc} + G_{coag} + G_{sg} + R_{charge}, \tag{7}$$

where the source terms on the right-hand side include a nucleation term J_{nuc}, growth terms for coagulation, G_{coag}, and for gas-phase surface deposition (surface growth), G_{sg}, and a term accounting for charge fluctuations, R_{charge}. Note that, by using a recombination rate, we also considered the recombination of ions and electrons on the surface of the dust particle, which represents an additional loss mechanism for plasma ions and electrons.

Once the large cluster's density exceeds a critical threshold, typically of the order of 10^{10} cm^{-3}–10^{11} cm^{-3}, the agglomeration phase of a nanoparticle starts. During coagulation, the particles quickly grow in time from a few nm to several tens of nanometers, as a result of the collision of two smaller nanoparticles. Aerosol physics will be a good technique for studying the coagulation of a particle, which lies in the free molecular regime (an excellent assumption for the conditions of interest). The free molecular regime has assumed spherical particles and unity sticking coefficients, and neglected the effect of van der Waals forces, thus the coagulation coefficient $\beta(v_i, v_j)$ between two interacting particles with a volume v_i and v_j can be written as

$$\beta(v_i, v_j) = (3/4\pi)^{1/6}(6k_B T/\rho_d)^{1/2}(1/v_j + 1/v_j)^{1/2} \times (v_i^{1/3} + v_j^{1/3})^2, \tag{8}$$

where ρ_d is the mass density of the material of which the particles are composed, k_B is the Boltzmann constant, and T is the absolute temperature. In the present paper, the smallest bin in the sectional model has a diameter of 1.0 nm, while the largest bin is 50.0 nm in diameter, corresponding to the volume section of 6.54×10^4 nm^3. The size domain is logarithmically divided into 40 sections for the volume domain, due to the

smaller energy and current for the large size nanoparticle. It should be mentioned that, by using the same temporal resolution, we also investigate the transport of nanoparticles in the coagulation module.

3. Numerical approach

In this paper, 125 grid points are employed in the axis direction, while two separate calculation cycles are implement in a time-stepping procedure, each with its own specific time-step. The radio frequency (RF) cycle is divided into 10^4 time-steps ($\Delta t \approx 7.4 \times 10^{-12}$ s), a longer time step of 7.4×10^{-9} s is adopted for the description of the neutral–neutral chemistry to speed up the calculation. The second calculation cycle with a larger time-step is introduced in the nanoparticle module, due to the large difference in timescale between the nanoparticle motion and the RF period. To avoid instabilities, we first move the total positive ion density with the same amount as the negatively charged nanoparticles to the new nanoparticle profiles before switching back to the next RF cycles.[22] This method reduces the computational effort and studies the discharge dynamics in a self-consistent way.

The numerical method used to treat the electrons differential equations is based on an implicit finite-difference technique using the Scharfetter—Gummel exponential scheme,[22] while the ions equations using the upwind scheme. Implicit time advancement is used for both the electron and ion equations. The discussion given below is based on the convergence of the fluid model, which ensures that the relative changes of the discharge parameters between two succeeding RF cycles are less than 10^{-4}.

4. Results and discussion

In this work, selected results presented here are computed for typical conditions that result in particle formation, by using a sectional mode. The RF source is applied on the upper showerhead electrode with a driving frequency of 13.56 MHz, while the lower electrode remains electrically grounded, and the gas pumping across the sidewall. The ideal showerhead is considered as a uniformly porous wall with a uniform gas flow into the reactor crossing its whole area. The ion temperature $T_{\rm ion} = 400$ K, and the electrode spacing $L = 3.0$ cm. In order to investigate the voltage, gas flow rate, and pressure dependence, the voltage will be varied between 80 V and 120 V, the gas flow rate varied between 20 sccm and 60 sccm, and the pressure varied between 300 mTorr and 600 mTorr (1 Torr = 1.33322×10^2 Pa), but for all other simulations, they are kept constant at the voltage 100 V, the gas pressure 300 mTorr, and the pure C_2H_2 flow rate 20 sccm.

In our simulation, without secondary electron emission, thus the results are limited to the α regime, where sheath oscillation is responsible for most of the electron heating in the discharge sustaining. This is a valid assumption for the considered conditions.[15]

Figure 1 illustrates the calculated time-averaged profiles of the electron density $n_{\rm e}$ and the most important electron temperature $T_{\rm e}$. As shown in Fig. 1(a), the resulting electron density exhibits a relatively high concentration (1.8×10^{10} cm^{-3}) in the bulk of the discharge between the two electrodes, but begins to oscillate obviously in the sheath regions during an RF cycle, resulting in an electric field effect. This can be further explained from Fig. 1(b) that the electron temperature keeps almost invariable, about 4.5 eV, within the bulk plasma and oscillates rapidly in the sheath regions due to the Ohmic heating.

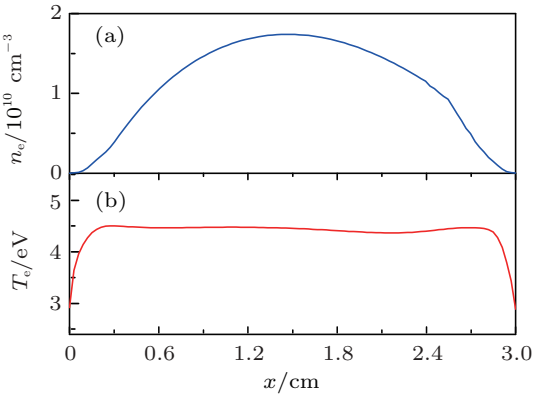


Fig. 1. (color online) The spatial variation profiles of the electron density and electron temperature, with $P = 300$ mTorr, $V_0 = 100$ V, $f = 13.56$ MHz, $\widehat{\nu} = 20$ sccm.

The negative species' densities within one RF period are plotted in Fig. 2. It is clear from the figure that two different chains of polymerization reactions, starting from C_2H^- and H_2CC^- can be distinguished, and H_2CC^- occupies a larger proportion, approximately 20 times higher than C_2H^-. This is due to the fact that H_2CC^- is more stable compared with the vinylidene neutral and stable with respect to autodetachment. As far as the anions are concerned, there are two major pathways which contribute to the generation of the $C_{2n}H^-$ ($n = 1$–6) anions: electron impact dissociation attachment reactions of $C_{2n}H_2$ ($n = 1$–6) molecules, and polymerization reactions of the smaller $C_{2n}H^-$ ($n = 1$–5) anions with C_2H_2. We can observe from the figure that the $C_{2n}H^-$ ($n = 1$–6) anions first increase with the C atom and reach a maximum value around 1.0×10^{10} cm^{-3} (C_6H^-), and then with the continuous increasing of the number of C atoms, the $C_{2n}H^-$ density decreases. This is due to the fact that the electron impact dissociative attachment of $C_{2n}H_2$ ($n < 4$) are the principal routes, while the polymerization reactions of smaller anions with C_2H_2 play a key role in the formation of the larger anions $C_{2n}H^-$ ($n = 4$–6)).

For the positive ions, only the most significant concentrations are represented in Fig. 3. As is clear from Fig. 3,

the major positive ion appears to be $C_4H_2^+$ with a density of about 6.0×10^8 cm^{-3}. As the electron impact ionization as well as molecules-cation reactions are two predominant routes for $C_{2n}H_m^+$ generation, once the contribution of the electron impact ionization of C_4H_2 is larger than the association reactions of smaller cations ($C_2H_2^+$) with C_2H_2, $C_4H_2^+$ density can be the highest. Note that, when the $C_{2n}H_m^+$ ($n > 2$) cations become bigger, the electron impact ionization reactions become less important as a production mechanism, and then the association reactions play a major role in the formation of larger cations $C_{2n}H_m^+$. Therefore, for $C_{2n}H_m^+$, it seems that the competition between the electron impact ionization and the association reactions will mainly determine the variation of the particles density. Our calculation is in good agreement with the results obtained in both the experimental measurements[8] and theoretical studies.[12]

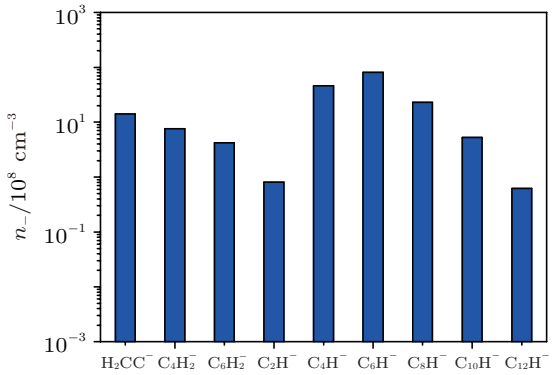


Fig. 2. (color online) The spatial variation profiles of the negative ions density within one RF period, with the settings being the same as those in Fig. 1.

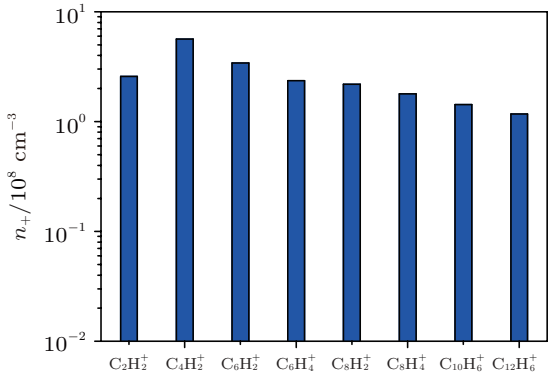


Fig. 3. (color online) The spatial variation profiles of the positive ions density within one RF period, with the settings being the same as those in Fig. 1.

Since the background gas balance equations are taken into account, we investigate the effect of the gas flow rate on the influence of the nanoparticle density. Here, we choose nanoparticles with diameter at $D_d = 10.0$ nm. Figure 4 shows the spatial variation profiles of the average nanoparticle density, with the pure C_2H_2 flow rate set at 20, 40, and 60 sccm. We can clearly see that the density profile of 10-nm particles exhibit a prominent peak near the upper electrode, even if the gas temperature has a relatively small variation, showing that the gas temperature has a significant effect on the spatial distribution profiles of particles in the submicrometer area. This is because the thermophoretic force really starts to dominate the transport of the 10-nm particles and drives them away from the heated electrode towards the cooled electrode, thus a dust particle will be suspended in some well-defined region of the plasma. We can also study the location of the particles growth much more clearly from Fig. 4 that, as the gas flow increases, the particles tend to move closer to the sheath boundary adjacent to the RF electrode. Moreover, as soon as the gas flow rate increases, the nanoparticle density increases since the gas temperature differences increase. Hence we can expect that the gas flow rate can be used as an efficient solution for the confinement of the contaminant dust particles, as it can suppress the particles to the cooled electrode.

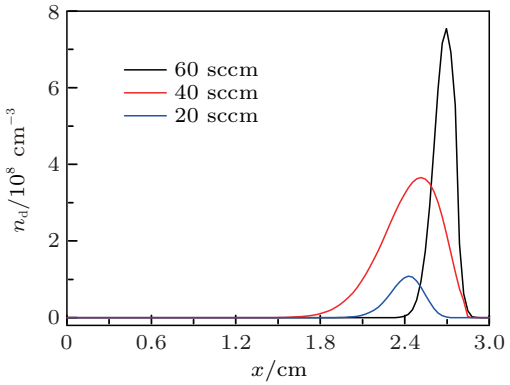


Fig. 4. (color online) The spatial variation profiles of the nanoparticle number density n_d within one RF period for different gas flows, $\hat{v} = 20$, 40, and 60 sccm, with $D_d = 10.0$ nm, $P = 300$ mTorr, $f = 13.56$ MHz, $V_{rf} = 100$ V.

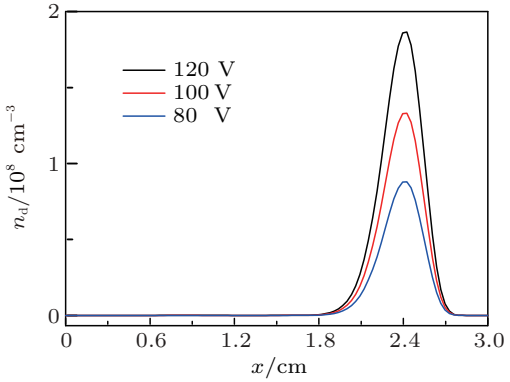


Fig. 5. (color online) The spatial variation profiles of the nanoparticle number density n_d within one RF period for different RF voltages, $V_{rf} = 80$, 100, and 120 V, with $D_d = 10.0$ nm, $P = 300$ mTorr, $f = 13.56$ MHz, $\hat{v} = 20$ sccm.

The effect of RF source voltage on the particle is also taken into account, as shown in Fig. 5, with the RF voltage V_{rf} set at 80, 100, and 120 V, while the particle size is 10 nm. It can be noticed from Fig. 5 that the RF voltage has a strong effect on the nanoparticle density profile, especially in the region of the nanoparticle density peak. By increasing the amplitude of the RF voltage, both the electron energy and plasma densities increase, so the nanoparticles get more energy when they

pass through the sheath of the upper electrode. Accordingly, an increase of the amplitude of the RF voltage leads to an increase in nanoparticle density.

Finally, we study the effect of gas pressure on the particle density profile. Figure 6 shows the size of 10-nm particle density at different pressures where $P = 300$, 500, 600 mTorr. One can observe that at the pressure of $P = 300$ mTorr, there is a prominent peak for the nanoparticle density near the upper electrode under the action of thermophoretic force. Moreover, as the pressure increases, the nanoparticle's average density in Fig. 6 moves nearer to the colder electrodes instead of just increasing, indicating that the collision frequency increases; furthermore, some neutral gases take part in more than one collision near the upper electrode and lose their energy after collisions. Therefore, the collision effect in the colder electrode becomes prominent, which drives the peak to gradually displace towards the colder electrode.

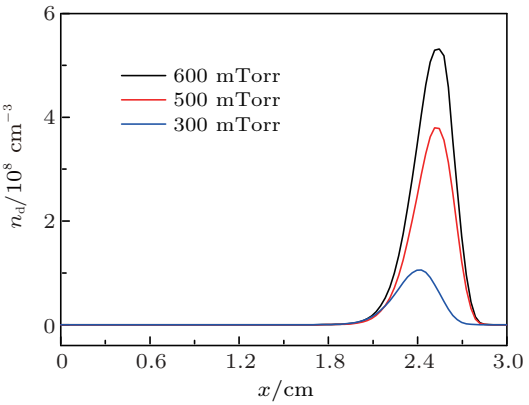


Fig. 6. (color online) The spatial variation profiles of the nanoparticle number density n_d within one RF period for different pressures, $P = 300$, 500, and 600 mTorr, with $D_d = 10.0$ nm, $V_{rf} = 100$ V, $f = 13.56$ MHz, $\widehat{v} = 20$ sccm.

5. Concluding remarks

In summary, we have studied the influences of the gas flow rate, the radio frequency source voltage, and the pressure on the formation of dust particles in RF capacitively coupled acetylene discharge by combining a self-consistent fluid model with an aerosol dynamics model. The absolute densities of nanoparticles grown via particle coagulation are presented for typical conditions of PECVD process variables. Since the neutral gas energy equation is taken into account, the effect of thermophoresis arising from a thermal gradient in gas temperature on the spatial distribution of coagulating nanoparticles has been evaluated. The simulation results indicate that the gas flow rate is an important parameter for the particle growth mechanism, which reveals the following features:

(i) Once the gas flow rate exists, the density profile of 10-nm particles shifts towards the cooler area at the plasma-sheath boundary adjacent to the powered electrode under the action of thermophoretic force.

(ii) By varying the gas flow rate, the density profile of 10-nm particles seems to gradually shift towards the cooler area at the upper showerhead electrode.

The effect of voltage and gas pressure on the nanoparticle density are also discussed, allowing us to know self-consistently the properties of the capacitively coupled acetylene discharge modulated by radio-frequency electric source. In future work, we will consider further the detailed coagulation process of nanoparticles in a two-dimensional fluid model.

References

[1] Grill A 1993 *Wear.* **168** 143
[2] Daniels B K, Brown D W and Kimock F M 1997 *J. Mater. Res.* **12** 2485
[3] Robertson J 2002 *Mater. Sci. Eng. R.* **37** 129
[4] Obraztsov A N, Volkov A P, Nagovitsyn K S, Nishimura K, Morisawa K, Nakano Y and Hiraki A 2002 *J. Phys. D: Appl. Phys.* **35** 357
[5] Vladimirov S V and Ostrikov K 2004 *Phys. Rep.* **393** 175
[6] Robertson J 1997 *Thin Solid Films* **296** 61
[7] Doyle J R 1997 *J. Appl. Phys.* **82** 4763
[8] Herrebout D, Bogaerts A, Gijbels R, Goedheer W J and Vanhulsel A 2003 *IEEE Trans. Plasma Sci.* **31** 659
[9] Stoykov S, Eggs C and Kortshagen U 2001 *J. Phys. D: Appl. Phys.* **34** 2160
[10] De Bleecker K, Bogaerts A and Goedheer W 2006 *Phys. Rev. E* **73** 026405
[11] Deschenaux Ch, Affolter A, Magni D, Hollenstein Ch and Fayet P 1999 *J. Phys. D: Appl. Phys.* **32** 1876
[12] Mao M, Benedikt J, Consoli A and Bogaerts A 2008 *J. Phys. D: Appl. Phys.* **41** 225201
[13] Warthesen S J and Girshick S L 2007 *Plasma Chem. Plasma Process.* **27** 292
[14] Ravi L and Girshick S L 2009 *Phys. Rev. E* **79** 026408
[15] Liu X M, Song Y H and Wang Y N 2005 *Phys. Rev. E* **71** 066405
[16] De Bleecker K, Bogaerts A and Goedheer W 2005 *Phys. Rev. E* **71** 066405
[17] Khan S A, Ali S and Mendonca J T 2013 *J. Plasma Phys.* **79** 973
[18] Crouseilles N, Hervieux P A and Manfredi G 2008 *Phys. Rev. B* **78** 155412
[19] Khan S A and Saleem H 2009 *Plasma Phys.* **16** 052109
[20] Hagelaar G J M, Fubiani G and Boeuf J-P 2011 *Plasma Sources Sci. Technol.* **20** 015001
[21] Hsu Cheng-Che, Nierode Mark A, Coburn John W and Graves David B 2006 *J. Phys. D: Appl. Phys.* **39** 3272
[22] De Bleecker K, Bogaerts A and Goedheer W 2006 *J. New Phys.* **8** 178